Hindawi
International Journal of Energy Research
Volume 2024, Article ID 8897089, 12 pages
https://doi.org/10.1155/2024/8897089

Research Article

Fabrication of 2D/2D $InVO_4/BiVO_4$ Heterojunction with Synergistic Effects for Enhanced Photocatalytic Degradation and Photoelectrochemical Applications

Hee Chang Jeon,[1] Ganesan Mohan Kumar,[1] Dong Jin Lee,[1] Sankar Sekar,[1,2] Deuk Young Kim,[1,2] and Pugazhendi Ilanchezhiyan[1]

[1]*Quantum Functional Semiconductor Research Center (QSRC), Institute of Future Technology, Dongguk University, Seoul, Republic of Korea*
[2]*Division of Physics and Semiconductor Science, Dongguk University, Seoul, Republic of Korea*

Correspondence should be addressed to Pugazhendi Ilanchezhiyan; ilancheziyan@dongguk.edu

Received 26 May 2023; Revised 7 November 2023; Accepted 20 April 2024; Published 10 May 2024

Academic Editor: Jiachao Peng

In this work, we report a novel 2D/2D $InVO_4/BiVO_4$ heterojunction nanocomposite constructed through a simple hydrothermal approach. The morphological analysis demonstrated that $BiVO_4$ nanoflakes to be anchored on the surface of $InVO_4$ nanosheets. The $InVO_4/BiVO_4$ heterojunction nanocomposite displayed increased light absorption promoting their visible light harvesting. The photoactivity of the prepared $InVO_4/BiVO_4$ heterojunction was explored for the degradation of tetracycline (TC) under light treatment. $InVO_4/BiVO_4$ heterojunction exhibited superior photocatalytic activity than that of bare $InVO_4$ and $BiVO_4$. The as-prepared $InVO_4/BiVO_4$ heterojunction photoanodes achieved a higher photocurrent density of 60 $\mu A/cm^2$ under illumination in 0.5 M Na_2SO_4 electrolyte. The enhanced photoelectrochemical performance is attributed to the synergistic effect and interface formation between $InVO_4$ and $BiVO_4$ and can effectively promote the charge separation and transfer of photoinduced carriers in heterojunction.

1. Introduction

Photocatalysis based on semiconductor materials is a kind of green technology that converts solar energy into chemical energy for water splitting, fixation of nitrogen, air purification, wastewater treatment, disinfection, and carbon dioxide reduction [1–6]. The crucial factors that affect the photocatalytic activities are utilization efficiency of solar energy, transfer and separation efficiency of photoinduced charge carriers, and redox ability [7]. Various strategies have been carried out to enhance the photoelectrochemical activities, such as defect engineering [8, 9], doping [10, 11], and heterojunction [12, 13]. Among various approaches, fabricating heterojunction with different semiconductors is a promising way to improve the utilization rate of solar energy and restrain recombination of photoinduced charge carriers [14–16].

As an important metal oxide semiconductor, bismuth vanadate ($BiVO_4$) was identified as one of the most appealing photocatalysts under visible light irradiation owing to its narrow bandgap energy (Eg = 2.40 eV), chemical stability, and nontoxicity [17–19]. Nevertheless, due to low separation efficiency of photoexcited charge carriers and poor charge deliver capacity, the photocatalytic performance of pure $BiVO_4$ is still unsatisfied. Hence, efforts are made in this work, to integrate $BiVO_4$ with other suitable materials for reactants accumulations and efficient charge transfer process [20–24]. The construction of heterostructure accelerates efficient charge transfer and facilitates the separation of photoinduced charge carriers and prolongs the life time of photogenerated carriers, enhancing the photocatalytic performance.

From this perspective, the introduction of indium vanadate ($InVO_4$) with unique geometrical and electronic characteristics

is considered to be a suitable choice [25]. Meanwhile, the conduction (CB) and valence band (VB) of $InVO_4$ are more negative than that of $BiVO_4$ [26, 27], and the matching of CB and VB levels between $BiVO_4$ and $InVO_4$ makes $InVO_4$ to be an ideal choice for constructing heterojunction with $BiVO_4$. Therefore, $InVO_4/BiVO_4$ heterojunction nanocomposite is expected to become an excellent photocatalyst with high activity.

In this work, $InVO_4/BiVO_4$ heterojunction nanocomposite with 2D/2D coupling interface was processed by one-step hydrothermal approach. The photoactivity of $InVO_4/BiVO_4$ heterojunction was assessed by photodegradation of tetracycline (TC) under visible light. As expected, $InVO_4/BiVO_4$ heterojunction displayed a significantly enhanced photocatalytic activity for TC removal compared to that of bare $InVO_4$ and $BiVO_4$. The $InVO_4/BiVO_4$ heterojunction photoanodes achieved a higher photocurrent density of 60 $\mu A/cm^2$ under illumination in 0.5 M Na_2SO_4 electrolyte. The enhanced photoelectrochemical activity is attributed to the synergistic effect and interface formation between $InVO_4$ (IVO) and $BiVO_4$ (BVO), which can effectively enhance the charge separation and transfer of photoinduced carriers in heterojunction.

2. Experimental Methods

2.1. Synthesis of $InVO_4/BiVO_4$ Nanocomposite. IVO/BVO composite was synthesized via a hydrothermal approach. First, 3.5 mmol of $BiCl_3$ and 2 mmol CTAB were added to 20 mL ethylene glycol to form homogeneous solution. The 7.5 mmol of Na_3VO_4 was added dropwise to the homogeneous solution and stirred for 30 min. Then, stoichiometric amount of $InVO_4$ nanosheets was added and ultrasonically mixed for 30 min with the above mixture. The solution was then sealed into a 30 mL Teflon autoclave and kept at 433 K for 3 h. The final powder was washed by ethyl alcohol and DI water and dried at 333 K for 12 h. The obtained $BiVO_4$ nanoflakes, $InVO_4$ nanosheets, and $InVO_4/BiVO_4$ heterojunction were referred as BVO, IVO, and IVO/BVO. The schematic illustration of the synthesis of $InVO_4/BiVO_4$ heterojunction is shown in Figure 1. The bare IVO nanosheets and BVO nanoflakes were synthesized under the same conditions and are provided in supporting information (available here).

3. Results and Discussions

SEM is employed to inspect the shape, microstructure, and morphology of the samples. As shown from Figures 2(a) and 2(b), the as-prepared IVO consists of a large number of wrinkled nanosheet-like morphology with smooth surface. In contrast, as-prepared BVO consisted of relatively smaller irregular flakes with a clean and smooth surface (Figures 2(c) and 2(d)). However, after the hydrothermal process in the presence of IVO nanosheets as the substrates, BVO nanoflakes were assembled on the surface of IVO nanosheets (Figures 2(e) and 2(f)). As seen from the image, the morphology of BVO and IVO architectures is retained in the final IVO/BVO nanocomposite. The SEM images confirmed that the 2D/2D IVO/BVO heterojunction was successfully synthesized. The morphological and structural details of the IVO/BVO heterojunction were further investigated using TEM and HRTEM. The TEM images shown in Figure S1a and S1b further illustrate that IVO and BVO possess nanosheet- and nanoflake-like morphology agreeing with SEM analysis. Figure 3(a) shows that TEM image of IVO/BVO heterojunction confirms the BVO nanoflakes to be loaded on the IVO nanosheets. It could be observed that the BVO nanoflakes are contacted tightly with IVO nanosheets. This could be beneficial for a smooth foundation for photogenerated charge carrier migration. HRTEM image of IVO/BVO heterojunction (Figure 3(b)) displays well-defined lattice spacing of about 0.161 nm and 0.358 nm, corresponding to (121) plane of BVO and (021) plane of IVO. The SAED pattern of IVO/BVO heterojunction displays well-defined spots, suggesting good crystalline nature of synthesized heterojunction (Figure 3(c)). In addition, EDX mapping performed on IVO/BVO heterojunction is illustrated in Figures 3(d)–3(h) and Figure S2. The four constituent elements In, Bi, V, and O of the IVO/BVO heterojunction are well detected uniformly throughout the heterojunction, and the quantitative atomic composition of each component in the samples is compared in Table S1.

The crystalline phase and structures of the as-prepared IVO, BVO, and IVO/BVO heterojunction were determined using XRD, as shown in Figure 4(a). The diffraction patterns of both IVO and BVO are well indexed to orthorhombic $InVO_4$ (JCPDS No. 00-048-0898) and monoclinic $BiVO_4$ (JCPDS No. 14-0688), confirming the successful synthesis of IVO/BVO heterojunction nanocomposite (Figure S3). The Raman spectrum was employed to investigate the change in the structural properties of bare IVO, BVO, and IVO/BVO heterojunction (Figure 4(b)). The spectrum of IVO shown in Figure 4(b) exhibited a strong mode at 910 cm^{-1}, which corresponds to vibrations of In-O bond in IVO [28]. Similarly, the modes at 393, 341, 207, and 135 cm^{-1} are related to stretching modes of V-O bond [29–31]. The Raman spectrum of BVO exhibits several modes at 210, 365, 327, and 815 cm^{-1} related to vibrations of the VO_4 tetrahedron [32, 33]. The sharp intense band at 825 cm^{-1} corresponds to symmetric stretching modes of V-O [34], and the weak bands at 365 cm^{-1} and 327 cm^{-1} were assigned to symmetric and asymmetric bending vibration modes of VO_4 tetrahedron [35]. Furthermore, the signals from IVO/BVO heterojunction confirm the coexistence of characteristic vibration modes related to BVO and IVO, thus certifying the successful synthesis of IVO/BVO heterojunction.

The variation in the surface states and chemical composition of IVO/BVO heterojunction was studied through XPS. Figure S4 displays survey spectrum of IVO/BVO heterojunction signifying the element signal of In, Bi, V, C, and O. The core level deconvoluted spectrum of Bi 4f, for both BVO and IVO/BVO heterojunction, is displayed in Figure 5(a). The binding energies at 157.04 eV (Bi $4f_{7/2}$) and 163.47 eV (Bi $4f_{5/2}$) reveal the Bi^{3+} valence state in BVO and IVO/BVO heterojunction [36–38]. Similarly, the deconvoluted doublet peaks of In 3d spectra (Figure 5(b)), at binding energies 444.4 eV (In $3d_{5/2}$) and 451.8 eV (In $3d_{3/2}$), reveal indium to exist in In^{3+} chemical state [39–41]. Meanwhile, the peak position of Bi 4f and In 3d peaks of IVO/BVO heterojunction exhibits a shift to higher

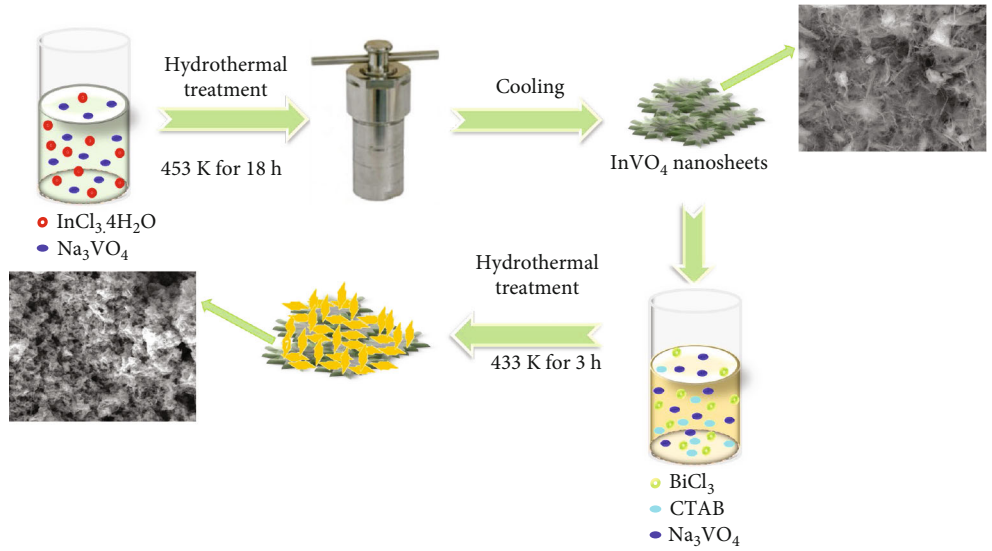

Figure 1: Schematic illustration for the formation of IVO/BVO heterojunction nanocomposites.

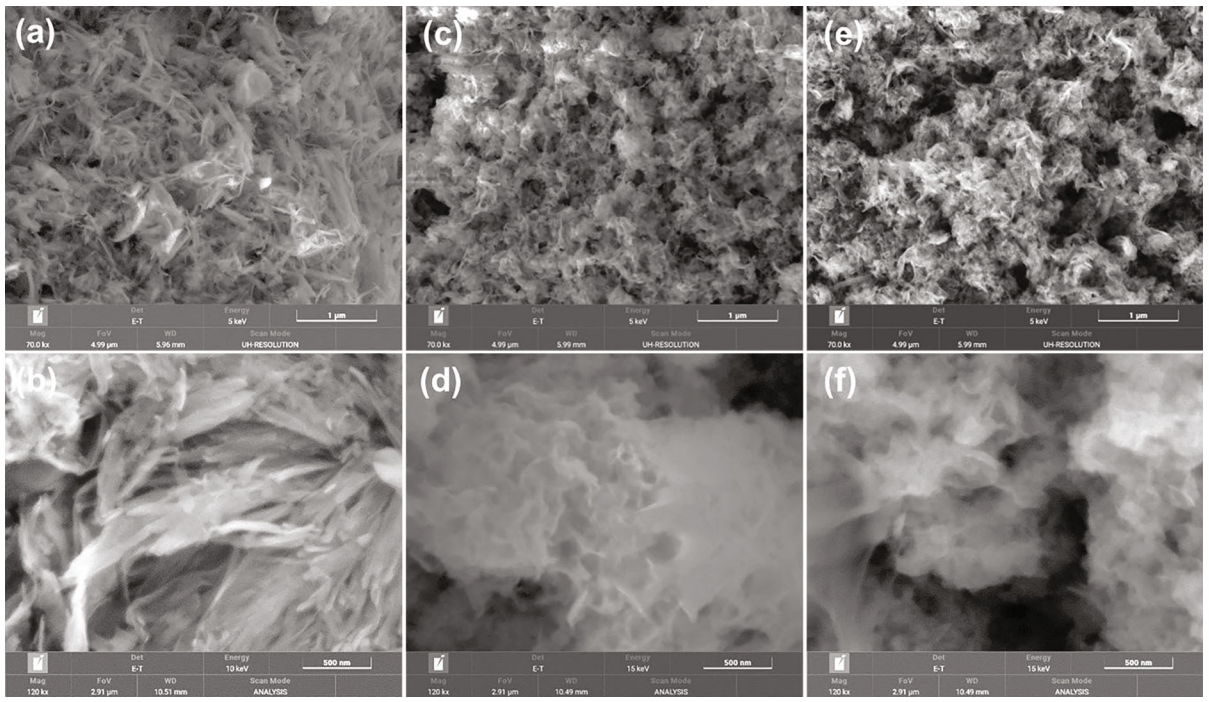

Figure 2: Morphological characterization of IVO/BVO heterojunction: (a, b) SEM images and of IVO nanosheets; (c, d) SEM images of BVO nanoflakes nanorods; (e, f) SEM images of IVO/BVO heterojunction.

binding energy, compared to bare IVO and BVO (Figure S5), suggesting electron transfer from IVO to BVO. The V 2p core level spectrum for IVO/BVO heterojunction is displayed in Figure 5(c). The spectra of V 2p were deconvoluted into three peaks at 517.60, 525.20, and 517.04 eV. The peaks at 517.60 eV (V $2p_{3/2}$) and 525.20 eV (V $2p_{1/2}$) correspond to V^{5+} states, based on the previous results [42–44]. In addition, the peak located at 517.04 eV is related to V $2p_{3/2}$ of V^{4+}. The spectra of O1s found to be deconvoluted to two peaks at 530.3 eV related to lattice oxygen in the nanocomposite and 531.6 eV related to surface hydroxyl groups (Figure 5(d)) [45–47]. The above results further confirm the heterojunction formation between IVO and BVO, which agrees with TEM and Raman results.

Preferable optical absorption characteristics have a direct impact on the photoelectrochemical activity of the semiconductors. UV-visible absorption spectrum was employed to attest the optical properties of the bare IVO, BVO, and

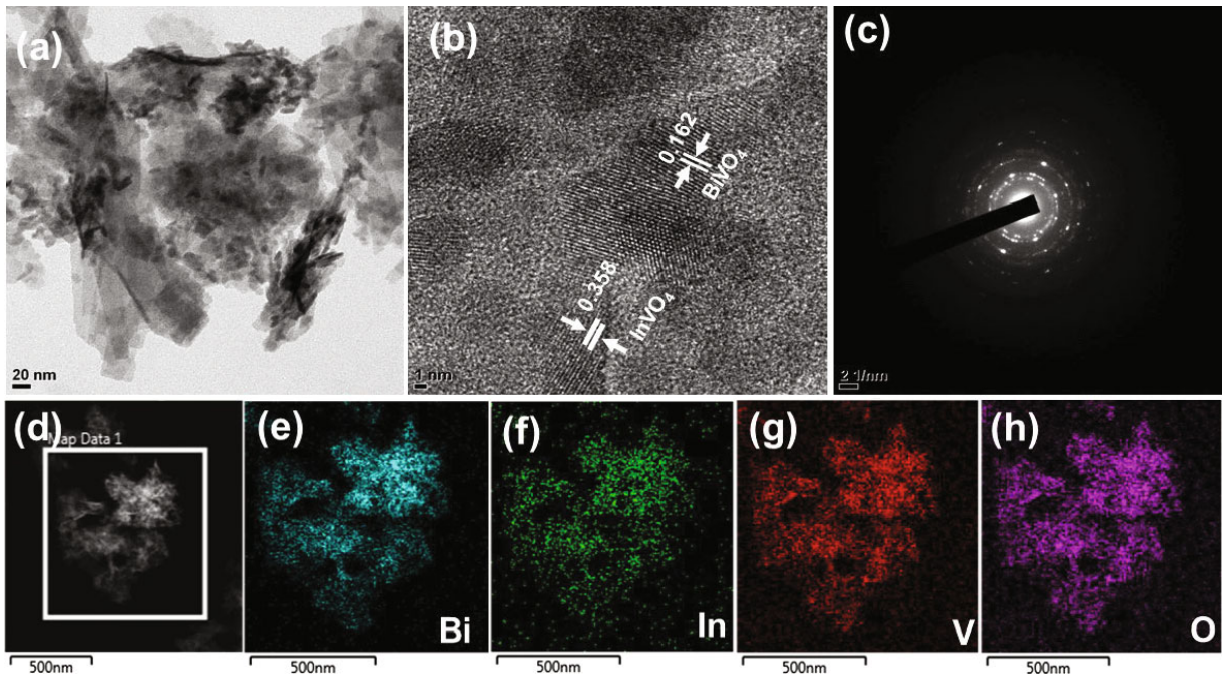

Figure 3: (a) TEM, (b) HRTEM image, and (c) SAED pattern of IVO/BVO heterojunction. (d–h) EDX elemental mapping of Bi, In, V, and O from selected area for IVO/BVO heterojunction.

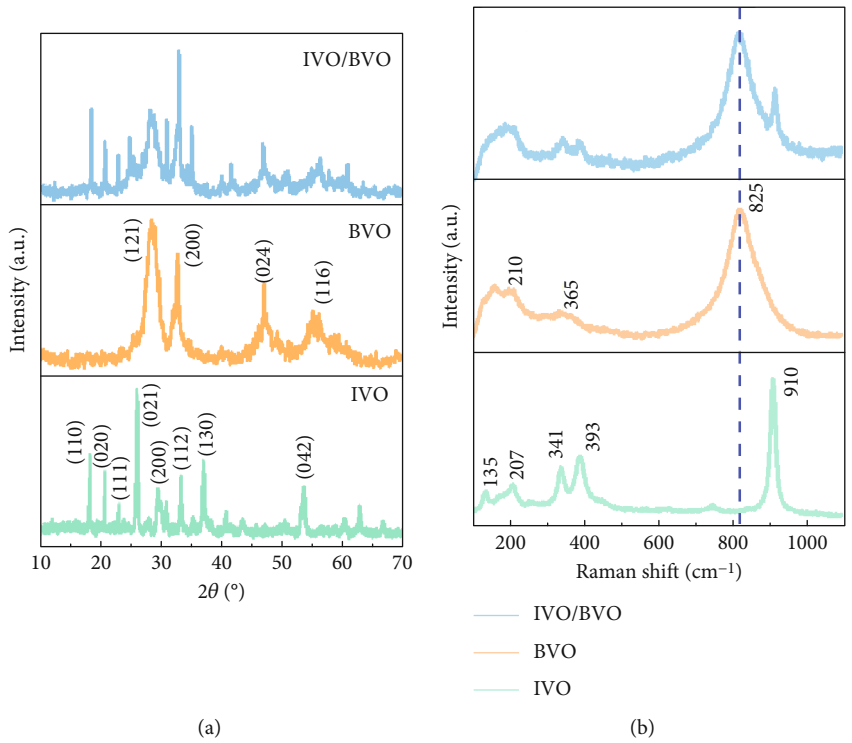

Figure 4: (a) XRD patterns and (b) Raman spectrum of IVO, BVO, and IVO/BVO heterojunction nanocomposite.

IVO/BVO heterojunction (Figure 6(a)). As shown in the figure, the bare IVO nanosheets exhibited an absorption edge at 452 nm and BVO nanoflakes at 460 nm. Meanwhile, the absorption spectrum of IVO/BVO heterojunction reveals an extended light absorption from 400 to 600 nm than bare IVO and BVO. This indicates that the introduction of IVO leads to enhancement of absorption ability in BVO. This effective change of the absorption spectra clearly indicates

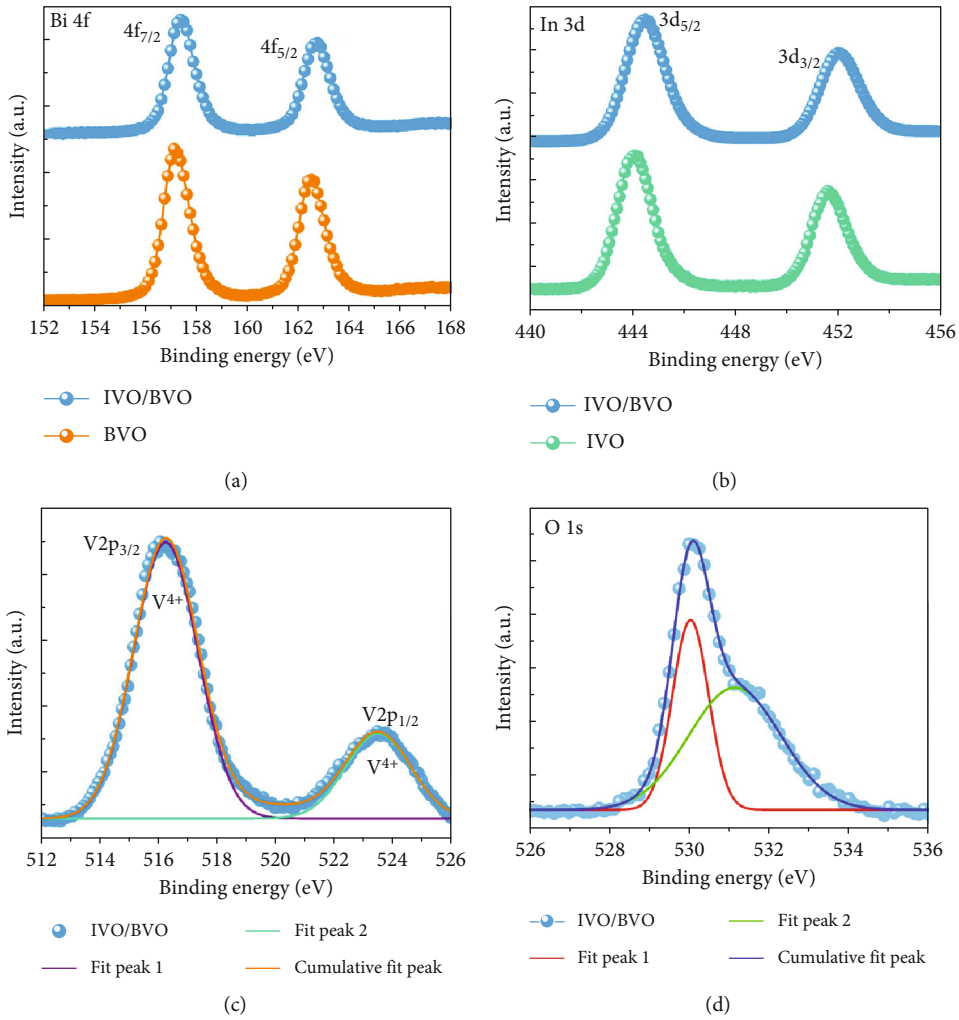

FIGURE 5: (a) XPS core level of Bi 4f spectra of bare BVO and IVO/BVO heterojunction nanocomposite. (b) XPS core level of In 3d spectra of bare IVO and IVO/BVO heterojunction composite. XPS core level of (c) V 2p and (d) O1s spectra of IVO/BVO heterojunction nanocomposite.

that the IVO/BVO heterojunction has wider spectral harvesting, efficiently leading to the enhancement of the photoelectrochemical activity. Using the absorption spectra, the bandgap (E_g) of IVO, BVO, and IVO/BVO heterojunction (Figures 6(b)–6(d)) was obtained via the Tauc plot, of $(\alpha h\upsilon)^2$ versus the photon energy ($h\upsilon$). According to the plot, the calculated bandgaps of IVO, BVO, and IVO/BVO heterojunction were 2.02 eV, 2.3 eV, and 2.27 eV, respectively. Additionally, we have carried out Mott-Schottky analysis to determine the band structure of IVO and BVO. Figures 6(e) and 6(f) show the Mott-Schottky (MS) plots of the IVO and BVO samples. The positive slopes of the MS plot suggest that both IVO and BVO are an *n*-type semiconductor. Moreover, the flat band potentials of IVO and BVO were estimated to be -0.56 V and -0.060 V. Depending on the MS plots, the conduction band potentials (E_{CB}) of IVO and BVO were derived to be -0.36 V and 0.13 V, respectively. Using the bandgap energies (E_g) obtained using the Tauc plots (Figures 6(b) and 6(c)), the valence band potentials (E_{VB}) were calculated from the formula $E_{CB} = E_{VB} - E_g$ to be 1.66 and 2.43 V for IVO and BVO, respectively.

The photoactivity of bare IVO, BVO, and IVO/BVO heterojunction nanocomposite was studied through degradation of tetracycline (TC) under visible light. The degradation rates of TC over bare IVO, BVO, and IVO/BVO heterojunction are displayed in Figure 7(a). The bare IVO and BVO exhibited photodegradation rate of 64% and 79% after 90 min of irradiation. However, the IVO/BVO heterojunction exhibited prominent degrade efficiency of 92%, which was 2- and 1.25-fold higher than the photodegradation for BVO and IVO (Figure 7(b)). The elevated photoactivity implies that the heterojunction formed between IVO and BVO played a major role in improving the photocatalytic activity. These results suggest a more efficient separation and transfer of photoinduced charge carriers to occur in the heterojunction, which could be attributed to the synergetic effect of IVO/BVO heterojunction structures. Furthermore, the extended light absorption ability of the nanocomposite in the visible

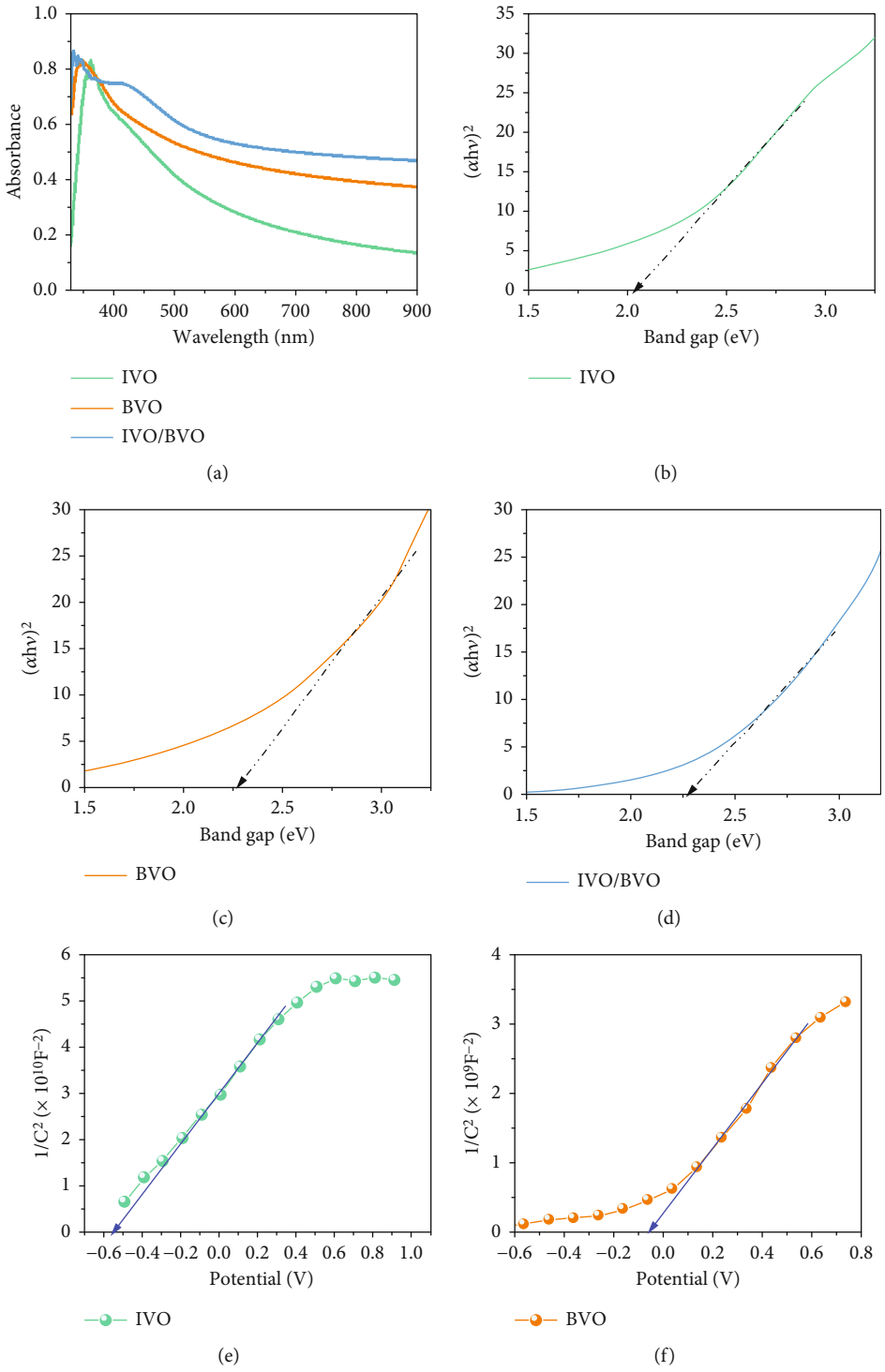

Figure 6: Optical properties of IVO/BVO heterojunction. (a) UV-vis absorption spectrum of bare IVO, BVO, and IVO/BVO heterojunction. Tauc's plot of (b) IVO nanosheets, (c) BVO nanoflakes, and (d) IVO/BVO heterojunction nanocomposite.

region provides a suitable band edge where the heterojunction interface can play a vital role in TC photodegradation. The photocatalytic degradation process of TC by IVO/BVO heterojunction was further evaluated using first-order kinetics and depicted in Figure 7(c). Clearly, IVO/BVO heterojunction displayed a higher rate constant value compared to bare IVO and BVO, demonstrating the superior photocatalytic activity of IVO/BVO heterojunction. The apparent rate constant values for IVO and BVO were 0.072 min^{-1} and 0.012 min^{-1}, respectively. However, IVO/BVO heterojunction possesses higher rate constant value (0.023 min^{-1}) of which is 3-fold and 2-fold higher than that of IVO and BVO (Figure 7(d)).

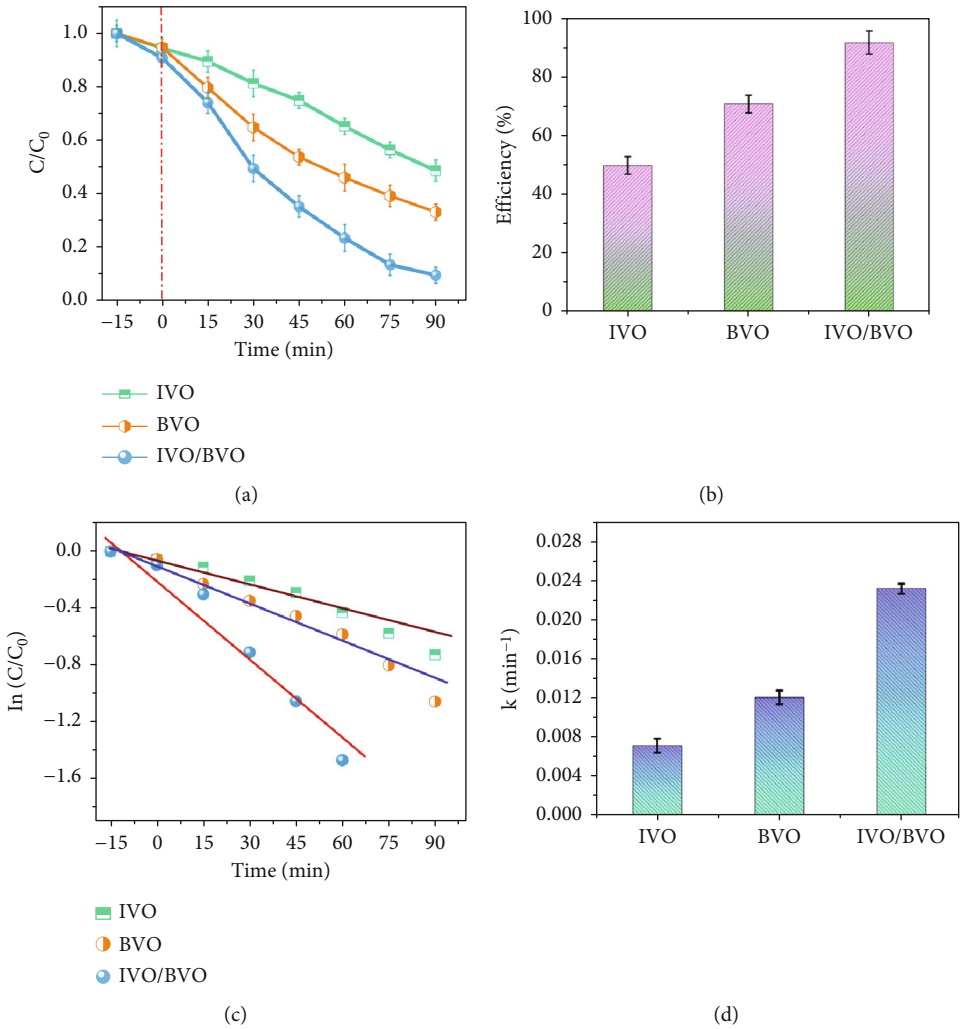

Figure 7: (a) Photocatalytic degradation of TC in presence of IVO, BVO, and IVO/BVO heterojunction nanocomposite under visible light irradiation. (b) Efficiency of photodegradation by IVO, BVO, and IVO/BVO heterojunction. (c) Photodegradation kinetic curves of TC in presence of IVO, BVO, and IVO/BVO heterojunction composite, where C_0 and C are the initial and instant concentrations of the TC, respectively. (d) Rate constant of photodegradation by IVO, BVO, and IVO/BVO heterojunction composite.

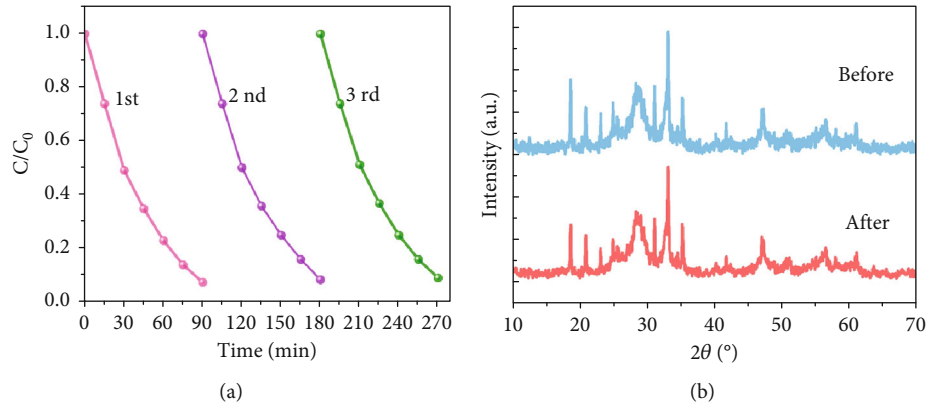

Figure 8: (a) Stability test over IVO/BVO heterojunction nanocomposite. (b) XRD patterns before and after degradation of the IVO/BVO heterojunction nanocomposite.

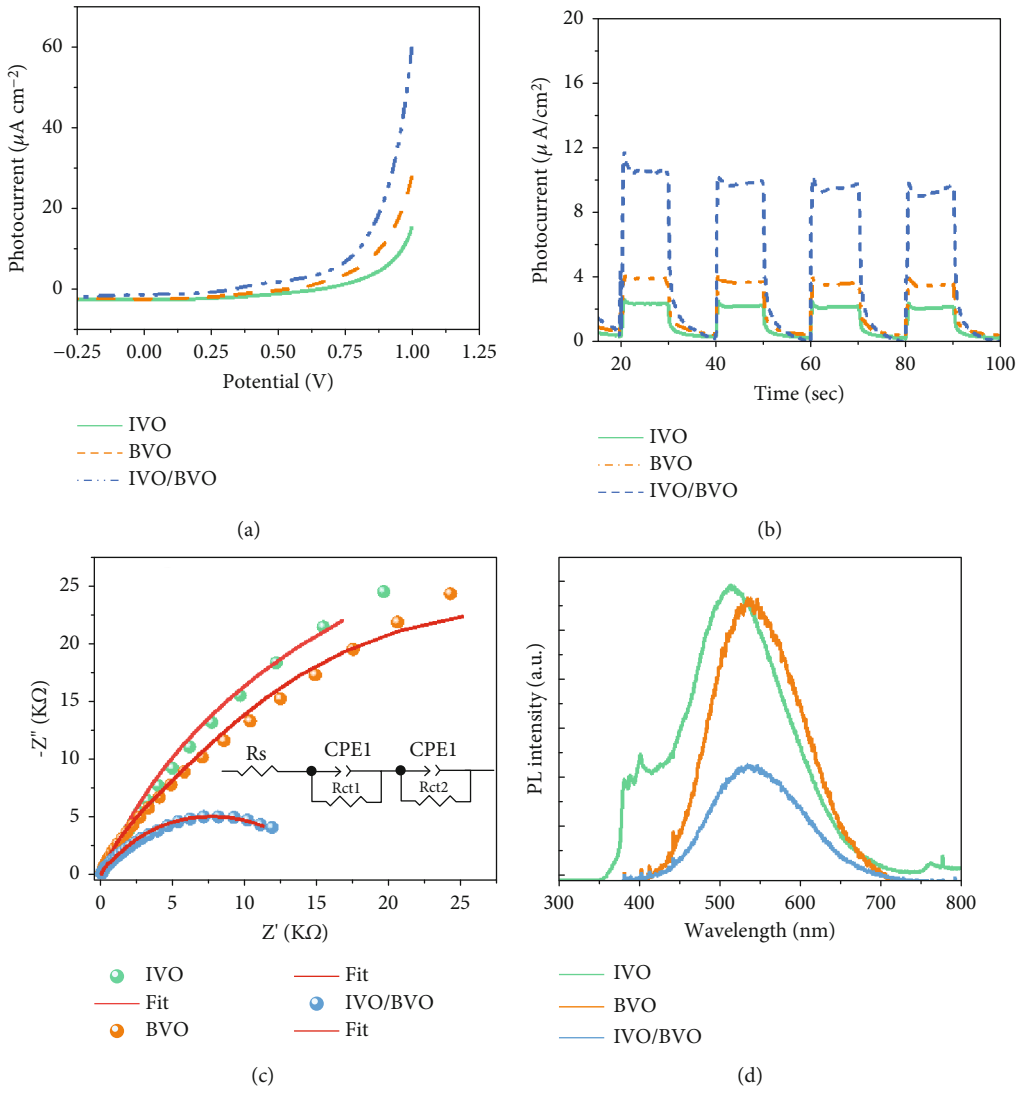

FIGURE 9: (a) LSV curve, (b) transient photocurrent responses, and (c) Nyquist impedance plots of IVO, BVO, and IVO/BVO heterojunction and (d) PL spectrum of IVO, BVO, and IVO/BVO heterojunction nanocomposite.

The above results suggest that the elevated photocatalytic degradation could be ascribed to the interfacial interactions and synergetic effects between IVO/BVO heterojunction. Furthermore, IVO/BVO heterojunction nanocomposite exhibits much higher photodegradation activity for TC comparably than those reported for BVO- and IVO-based photocatalysts (Table S2).

Additionally, the reaction mechanism on IVO/BVO heterojunction was explored by carrying out the scavenger test using various radicals, and the data are displayed in Figure S6. In this study, four scavengers BQ, IPA, and EDTA were used as quenchers for $\cdot O_2^-$, $\cdot OH$, and h^+, respectively. Figure S5 depicts the photodegradation kinetics of IVO/BVO heterojunction with different scavengers. As shown in Figure S5, the addition of IPA scavengers slightly suppressed the degradation efficiency of TC. However, the photocatalytic efficiency of TC is significantly inhibited with the introduction of EDTA and BQ, confirming the major role of h^+ and $\cdot O_2^-$ in the degradation process. The above results suggest that h^+, $\cdot O_2^-$, and $\cdot OH$ are major active species and h^+ and $\cdot O_2^-$ played crucial role in TC degradation process.

The reusability and stability of the IVO/BVO heterojunction nanocomposite were tested through three cycling experiments under irradiation as shown in Figure 8(a). The results illustrate a little loss of degradation efficiency of heterojunction nanocomposite after three successive cycles. The samples of IVO/BVO heterojunction nanocomposite before or after photocatalytic reaction were characterized by XRD analysis. Figure 8(b) shows the XRD patterns before and after degradation of the IVO/BVO heterojunction nanocomposite. It could be found that the XRD pattern of the recycled IVO/BVO heterojunction composite had almost no obvious difference compared with the unirradiated one. The results show that the photocatalyst is stable during the photocatalytic degradation process. Hence, this finding indicated that IVO/BVO heterojunction nanocomposite holds excellent stability for TC removal.

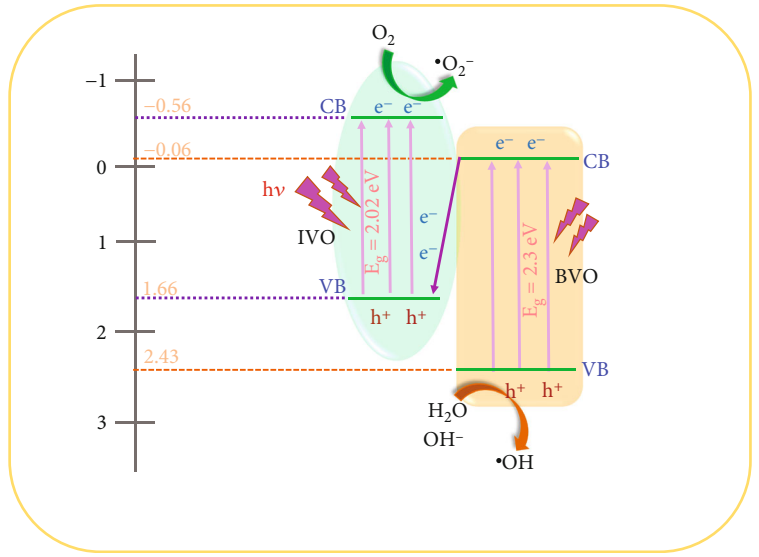

Figure 10: Schematic illustration of band diagram in IVO/BVO heterojunction.

The photoelectrochemical (PEC) ability of bare IVO, BVO, and IVO/BVO heterojunction nanocomposite was examined by measuring the linear sweep voltammetry (LSV) and transient photocurrent responses vs. time. The combination of IVO and BVO heterojunction exhibits attractive features for improved PEC performance, compared to bare IVO and BVO. Figure 9(a) displays the typical LSV plots of IVO, BVO, and IVO/BVO heterojunction photoanodes across a potential window of -0.2 to 1.0 V vs. Ag/AgCl under light conditions (100 mW/cm^2). Here, under light illumination, the photocurrents of both IVO and BVO photoanodes increase with increase in applied potential. For bare IVO and BVO, the onset potential was measured to be 0.33 V and 0.27 V vs. Ag/AgCl. The photocurrent density of IVO and BVO was measured to be 18 μA/cm^2 and 30 μA/cm^2 at 1.0 V. Interestingly, the photocurrent density of IVO/BVO heterojunction photoanodes reaches a maximum of 60 μA/cm^2 at 1.0 V, which is nearly 3-2-fold higher than bare IVO and BVO. The elevated photocurrent density may be ascribed to enhance light absorption in the visible region and charge separation at the interface between IVO nanosheets and BVO nanoflakes. Furthermore, the onset potential of IVO/BVO heterojunction shows a cathodic shifts towards lower potential value, indicating the smaller driving force required to initiate the water splitting process. This is ascribed to the formation of IVO/BVO heterojunction for establishing the efficient charge transfer.

The photocurrent vs. time measurements of bare IVO, BVO, and IVO/BVO heterojunction photoanodes with repetitive light switching on/off cycles are illustrated in Figure 9(b). Here, the photocurrent of all the samples rapidly switches between on and off states. Among the three samples, the photocurrent response of IVO/BVO heterojunction was highest, about 1-2-fold higher than bare IVO and BVO, demonstrating the enhanced photoelectric conversion efficiency in heterojunction. Furthermore, the photocurrent response of the IVO/BVO heterojunction photoelectrodes produces stable and reproducible photocurrent of 6 μA/cm^2 over several on/off cycles, indicating good stability from the heterojunction.

Meanwhile, EIS was further employed to study the efficient charge transfer process on bare IVO, BVO, and IVO/BVO heterojunction electrodes. In general, charge transfer resistance (R_{ct}) is equivalent to the diameter of arc radius in Nyquist plot, and in the present studies, a smaller arc radius represents lower resistance for higher charge transfer efficiency [48, 49]. Nyquist curve of bare IVO, BVO, and IVO/BVO heterojunction electrodes is presented in Figure 9(c). All three electrodes are modeled with equivalent circuit (inset Figure 9(c)), and the fitted values of R_s, R_{ct1}, and R_{ct2} are summarized in Table S3. Compared to bare IVO and BVO, it was evident that the electrode arc radius for IVO/BVO heterojunction was significantly reduced, indicating improved separation and elevated interfacial charge transfer of photogenerated charge carriers. This is in consistent with photocurrent measurement results.

Photoluminescence (PL) spectrum was performed to investigate the recombination efficacy of charge carriers in IVO, BVO, and IVO/BVO heterojunction. Figure 9(d) illustrates PL results of pristine IVO, BVO, and IVO/BVO heterojunction. As shown in the PL spectra, both IVO and BVO display an intense emission band located at around 530 nm and 535 nm, which was mainly attributed due to the emission during the electron-hole recombination process. In contrast, PL intensity obviously decreases for IVO/BVO heterojunction than those of individual IVO and BVO. The reduction in PL intensity manifests the recombination rate of photogenerated charge carriers effectively to be suppressed in IVO/BVO heterojunction and results with the higher photocatalytic and photoelectrochemical activity [50–52].

Based on the band structure results obtained from the MS plot (Figures 6(e) and 6(f)) of IVO and BVO, the position of conduction and valence bands suggests that either type-II heterojunction or Z-scheme migration is possible. The C_B and V_B

potentials were estimated to be -0.36 V and 1.66 V for IVO and -0.06 eV and 2.43 eV for BVO, respectively. Since the C_B of IVO is lower than BVO, the photoinduced electrons (e^-) generated on the C_B of IVO move to the C_B of BVO. On the other hand, the photoexcited (h^+) on the V_B of BVO transfers to the V_B of IVO. As a result, electrons gather on the C_B of BVO and holes accumulate on the V_B of IVO. However, the E_{CB} of BVO is weaker than the redox potential of $O_2/{}^{\cdot}O_2^-$ (-0.33 eV); the generation of ${}^{\cdot}O_2^-$ is forbidden. Similarly, the V_B of IVO (1.66 V) is more negative than the oxidation potential of $H_2O/{}^{\cdot}OH$ or $OH^-/{}^{\cdot}OH$ (1.99 V), and thus, no ${}^{\cdot}OH$ could be generated. Through the scavenger test experiment, it was detected that the system contained h^+, $\cdot O_2^-$, and ${}^{\cdot}OH$. Therefore, the traditional type-II mechanism is impossible to happen, and therefore, *Z*-scheme migration was put forwarded. As depicted in Figure 10, the photoinduced electrons on the C_B of BVO are moved to the V_B of IVO and then recombine quickly with the holes of IVO, resulting in higher separation rate of electron-hole pairs. Meanwhile, the electrons accumulated in C_B of IVO can combine with O_2 in water to form $\cdot O_2^-$, while the holes gathered in the V_B of BVO can react with H_2O/OH^- to yield ·OH. The h^+, $\cdot O_2^-$, and ${}^{\cdot}OH$ generated in the *Z*-scheme heterojunction are all involved in the removal of TC. The specific photogenerated electron-hole pair generation and reaction process are as follows:

$$\begin{aligned}
\mathrm{IVO} + h\nu &\longrightarrow \mathrm{IVO}\,(e^-) + \mathrm{IVO}\,(h^+)\\
\mathrm{BVO} + h\nu &\longrightarrow \mathrm{BVO}\,(e^-) + \mathrm{BVO}\,(h^+)\\
\mathrm{IVO}\,(h^+) + \mathrm{BVO}\,(e^-) &\longrightarrow \text{recombination}\\
\mathrm{IVO}\,(e^-) + O_2 &\longrightarrow \cdot O_2^-\\
\mathrm{BVO}\,(h^+) + H_2O &\longrightarrow {}^{\cdot}OH\\
\mathrm{BVO}\,(h^+) + OH^- &\longrightarrow {}^{\cdot}OH\\
(h^+, {}^{\cdot}OH, \cdot O_2^-) + \mathrm{TC} &\longrightarrow \text{photodegradation products}
\end{aligned} \tag{1}$$

4. Conclusion

In nutshell, a novel IVO/BVO nanocomposite with 2D/2D heterojunction was successfully synthesized through a hydrothermal method. The morphological and optical properties of IVO/BVO heterojunction nanocomposite were studied in detail. The heterojunction formation between IVO nanosheets and BVO nanoflakes was identified using HRTEM. The IVO/BVO heterojunction nanocomposite revealed enhanced absorption in the visible region. Furthermore, the IVO/BVO nanocomposite displayed enhanced photocatalytic performances than those of bare IVO and BVO upon illumination. Higher photocurrent density of 60 $\mu A/cm^2$ was obtained for IVO/BVO photoanodes than that for bare IVO (18 $\mu A/cm^2$) and BVO (30 $\mu A/cm^2$) under illumination. The elevated photoelectrochemical activity of the IVO/BVO nanocomposite is attributed to the heterojunction formation between IVO and BVO, resulting from the effective charge carrier separation. This finding provides a facile way to design and construct an efficient heterojunction nanocomposite photocatalysts for degradation of TC in aqueous system.

Data Availability

The data used to support the findings of this study included within the article and supporting information are available from the corresponding author upon reasonable request.

Conflicts of Interest

The authors declare no competing interests.

Acknowledgments

This research was funded by the National Research Foundation of Korea (NRF) grant funded by the Korea government (MSIT) (nos. 2022R1F1A1066650, 2021R1F1A1045642, and 2016R1A6A1A03012877).

Supplementary Materials

Characterization details, EDX spectra of IVO/BVO heterojunction, XPS survey spectrum of IVO/BVO heterojunction, PXRD pattern of IVO/BVO heterojunction, Bi 4f core level spectra of BVO and IVO/BVO heterojunction, photocatalytic degradation of TC over IVO/BVO heterojunction in the presence of different scavengers, comparison table for photodegradation activities of IVO/BVO heterojunction, R_s and R_{ct} values obtained from fitted equivalent circuit for IVO, BVO, and IVO/BVO heterojunction. *(Supplementary Materials)*

References

[1] C. B. Ong, L. Y. Ng, and A. W. Mohammad, "A review of ZnO nanoparticles as solar photocatalysts: synthesis, mechanisms and applications," *Renewable and Sustainable Energy Reviews*, vol. 81, pp. 536–551, 2018.

[2] W. Wang, R. Yang, T. Li, S. Komarneni, and B. Liu, "Advances in recyclable and superior photocatalytic fibers: material, construction, application and future perspective," *Composites Part B: Engineering*, vol. 205, article 108512, 2019.

[3] B. Sun, W. Zhou, H. Li et al., "Synthesis of particulate hierarchical tandem heterojunctions toward optimized photocatalytic hydrogen production," *Advanced Materials*, vol. 30, no. 43, article e1804282, 2018.

[4] B. Fang, Z. Xing, W. Kong, Z. Li, and W. Zhou, "Electron spin polarization-mediated charge separation in Pd/CoP@CoNiP superstructures toward optimized photocatalytic performance," *Nano Energy*, vol. 101, article 107616, 2022.

[5] Y. Wang, M. Liu, C. Wu et al., "Hollow nanoboxes Cu2-xS@ZnIn2S4Core-Shell S-scheme heterojunction with broad-spectrum response and enhanced photothermal-photocatalytic performance," *Small*, vol. 18, no. 31, article 2202544, 2022.

[6] Y. Chen, M. Cheng, C. Lai et al., "The collision between g-C_3N_4 and QDs in the fields of energy and environment: synergistic effects for efficient photocatalysis," *Small*, vol. 19, no. 14, article e2205902, 2023.

[7] J. Schneider, M. Matsuoka, M. Takeuchi et al., "Understanding TiO_2 photocatalysis: mechanisms and materials," *Chemical Reviews*, vol. 114, no. 19, pp. 9919–9986, 2014.

[8] C. Yang, Y. Zhu, J. Liu et al., "Defect engineering for electrochemical nitrogen reduction reaction to ammonia," *Nano Energy*, vol. 77, article 105126, 2020.

[9] D. Yan, H. Li, C. Chen, Y. Zou, and S. Wang, "Defect engineering strategies for nitrogen reduction reactions under ambient conditions," *Small Methods*, vol. 3, no. 6, article 1800331, 2019.

[10] C. Venkata Reddy, R. Reddy Kakarla, J. Shim, R. R. Zairov, and T. M. Aminabhavi, "Hydrothermally derived Cr-doped SnO_2 nanoflakes for enhanced photocatalytic and photoelectrochemical water oxidation performance under visible light irradiation," *Environmental Research*, vol. 217, article 114672, 2023.

[11] C. Venkata Reddy, I. Neelakanta Reddy, K. Ravindranadh, K. Raghava Reddy, J. Shim, and B. Cheolho, "Au-doped $BiVO_4$ nanostructure-based photoanode with enhanced photoelectrochemical solar water splitting and electrochemical energy storage ability," *Applied Surface Science*, vol. 545, article 149030, 2021.

[12] P. Dumrongrojthanath, A. Phuruangrat, K. Doungarno, T. Thongtem, P. Patiphatpanya, and S. Thongtem, "Microwave-hydrothermal synthesis of $BiOBr/Bi_2WO_6$ nanocomposites for enhanced photocatalytic performance," *Ceramics International*, vol. 44, pp. S148–S151, 2018.

[13] X. Lin, X. Guo, W. Shi, L. Zhao, Y. Yan, and Q. Wang, "Ternary heterostructured $Ag–BiVO_4/InVO_4$ composites: synthesis and enhanced visible-light-driven photocatalytic activity," *Journal of Alloys and Compounds*, vol. 635, pp. 256–264, 2015.

[14] J. Low, J. Yu, M. Jaroniec, S. Wageh, and A. A. Al-Ghamdi, "Heterojunction photocatalysts," *Advanced Materials*, vol. 29, no. 20, article 1601694, 2017.

[15] S. Le, T. Jiang, Y. Li et al., "Highly efficient visible-light-driven mesoporous graphitic carbon nitride/ZnO nanocomposite photocatalysts," *Applied Catalysis B, Environmental*, vol. 200, pp. 601–610, 2017.

[16] H. Y. Zhu, L. Xiao, R. Jiang, G. M. Zeng, and L. Liu, "Efficient decolorization of azo dye solution by visible light-induced photocatalytic process using SnO_2/ZnO heterojunction immobilized in chitosan matrix," *Chemical Engineering Journal*, vol. 172, no. 2-3, pp. 746–753, 2011.

[17] R. Koutavarapu, W. Y. Jang, M. C. Rao, M. Arumugam, and J. Shim, "Novel $BiVO_4$-nanosheet-supported MoS_2-nanoflake-heterostructure with synergistic enhanced photocatalytic removal of tetracycline under visible light irradiation," *Chemosphere*, vol. 305, article 135465, 2022.

[18] G. S. Kamble and Y.-C. Ling, "Solvothermal synthesis of facet-dependent $BiVO_4$ photocatalyst with enhanced visible-light-driven photocatalytic degradation of organic pollutant: assessment of toxicity by zebrafish embryo," *Scientific Reports*, vol. 10, no. 1, article 12993, 2020.

[19] Z. Zhang, M. Wang, W. Cui, and H. Sui, "Synthesis and characterization of a core–shell $BiVO_4$@g-C_3N_4 photo-catalyst with enhanced photocatalytic activity under visible light irradiation," *RSC Advances*, vol. 7, no. 14, pp. 8167–8177, 2017.

[20] G. Lu, Z. S. Lun, H. Y. Liang, H. Wang, Z. Li, and W. Ma, "In situ fabrication of $BiVO_4$- $CeVO_4$ heterojunction for excellent visible light photocatalytic degradation of levofloxacin," *Journal of Alloys and Compounds*, vol. 772, pp. 122–131, 2019.

[21] Y. Wen, Y. Zhao, M. Guo, and Y. Xu, "Synergetic effect of Fe_2O_3 and $BiVO_4$ as photocatalyst nanocomposites for improved photo-Fenton catalytic activity," *Journal of Materials Science*, vol. 54, no. 11, pp. 8236–8246, 2019.

[22] R. Yang, Z. Zhu, C. Hu et al., "One-step preparation (3D/2D/2D) $BiVO_4/FeVO_4$@rGO heterojunction composite photocatalyst for the removal of tetracycline and hexavalent chromium ions in water," *Chemical Engineering Journal*, vol. 390, article 124522, 2020.

[23] Y. Wang, K. Ding, R. Xu et al., "Fabrication of $BiVO_4/BiPO_4$/GO composite photocatalytic material for the visible light-driven degradation," *Journal of Cleaner Production*, vol. 247, article 119108, 2020.

[24] Y. Wang, D. Yu, W. Wang et al., "Synthesizing Co_3O_4-$BiVO_4$/g-C_3N_4 heterojunction composites for superior photocatalytic redox activity," *Separation and Purification Technology*, vol. 239, article 116562, 2020.

[25] Y. D. Meng, Y. Z. Hong, C. Y. Huang, and W. D. Shi, "Fabrication of novel Z-scheme $InVO_4$/CdS heterojunctions with efficiently enhanced visible light photocatalytic activity," *CrystEngComm*, vol. 19, no. 6, pp. 982–993, 2017.

[26] Y. L. Min, K. Zhang, Y. C. Chen, and Y. G. Zhang, "Sonodegradation and photodegradation of methyl orange by $InVO_4$/TiO_2 nanojunction composites under ultrasonic and visible light irradiation," *Ultrasonics Sonochemistry*, vol. 19, no. 4, pp. 883–889, 2012.

[27] S. W. Cao, Z. Yin, J. Barber, F. Y. C. Boey, S. C. J. Loo, and C. Xue, "Preparation of Au-$BiVO_4$ heterogeneous nanostructures as highly efficient visible-light photocatalysts," *ACS Applied Materials & Interfaces*, vol. 4, no. 1, pp. 418–423, 2012.

[28] Z. Kong, Y. J. Yuan, D. Chen et al., "Noble-metal-free MoS_2 nanosheet modified- $InVO_4$ heterostructures for enhanced visible-light-driven photocatalytic H_2 production," *Dalton Transactions*, vol. 46, no. 7, pp. 2072–2076, 2017.

[29] W. Ding, X. Lin, G. Ma, and Q. Lu, "Designed formation of $InVO_4/CeVO_4$ hollow nanobelts with Z-scheme charge transfer: synergistically boosting visible-light-driven photocatalytic degradation of tetracycline," *Journal of Environmental Chemical Engineering*, vol. 8, no. 6, article 104588, 2020.

[30] S. Cipagauta-Diaz, A. Estrella-Gonzalez, and R. Gomez, "Heterojunction formation on $InVO_4$/N-TiO_2 with enhanced visible light photocatalytic activity for reduction of 4-NP," *Materials Science in Semiconductor Processing*, vol. 89, pp. 201–211, 2019.

[31] H. Y. Hafeez, S. K. Lakhera, M. Ashokkumar, and B. Neppolian, "Ultrasound assisted synthesis of reduced graphene oxide (rGO) supported $InVO_4$-TiO_2 nanocomposite for efficient hydrogen production," *Ultrasonics Sonochemistry*, vol. 53, pp. 1–10, 2019.

[32] S. S. Mali, G. R. Park, H. Kim, H. H. Kim, J. V. Patil, and C. K. Hong, "Synthesis of nanoporous Mo:BiVO4thin film photoanodes using the ultrasonic spray technique for visible-light water splitting," *Nanoscale Advances*, vol. 1, no. 2, pp. 799–806, 2019.

[33] L. S. Kumari, P. P. Rao, A. N. P. Radhakrishnan, V. James, S. Sameera, and P. Koshy, "Brilliant yellow color and enhanced NIR reflectance of monoclinic $BiVO_4$ through distortion in VO_4^{3-} tetrahedra," *Solar Energy Materials & Solar Cells*, vol. 112, pp. 134–143, 2013.

[34] V.-I. Merupo, S. Velumani, K. Ordon, N. Errien, J. Szaded, and A.-H. Kassiba, "Structural and optical characterization of ball-milled copper-doped bismuth vanadium oxide ($BiVO_4$)," *CrystEngComm*, vol. 17, no. 17, pp. 3366–3375, 2015.

[35] C. Yin, S. Zhu, and D. Zhang, "3D nanostructured WO_3/$BiVO_4$ heterojunction derived from Papilio paris for efficient

water splitting," *RSC Advances*, vol. 7, no. 44, pp. 27354–27360, 2017.

[36] X. Wang, Y. Wang, M. Gao et al., "$BiVO_4/Bi_4Ti_3O_{12}$ heterojunction enabling efficient photocatalytic reduction of CO_2 with H_2O to CH_3OH and CO," *Applied Catalysis B, Environmental*, vol. 270, article 118876, 2020.

[37] B. Zhang, L. Chou, and Y. Bi, "Tuning surface electronegativity of $BiVO_4$ photoanodes toward high-performance water splitting," *Applied Catalysis B, Environmental*, vol. 262, article 118267, 2020.

[38] M. Noor, F. Sharmin, M. A. Al Mamun, S. Hasan, M. A. Hakim, and M. A. Basith, "Effect of Gd and Y co-doping in $BiVO_4$ photocatalyst for enhanced degradation of methylene blue dye," *Journal of Alloys and Compounds*, vol. 895, article 162639, 2022.

[39] G. Mohan Kumar, P. Ilanchezhiyan, A. Madhan Kumar et al., "Chemically-derived CuO/In_2O_3-based nanocomposite for diode applications," *CrystEngComm*, vol. 17, no. 31, pp. 5932–5939, 2015.

[40] P. Ilanchezhiyan, G. Mohan Kumar, F. Xiao et al., "Surface induced charge transfer in $Cu_xIn_{2-x}S_3$ nanostructures and their enhanced photoelectronic and photocatalytic performance," *Solar Energy Materials & Solar Cells*, vol. 191, pp. 100–107, 2019.

[41] J. Li, M. Zheng, F. Wei et al., "Fe doped $InVO_4$ nanosheets with rich surface oxygen vacancies for enhanced electrochemical nitrogen fixation," *Chemical Engineering Journal*, vol. 431, article 133383, 2022.

[42] G. Mohan Kumar, P. Ilanchezhiyan, H. D. Cho, D. J. Lee, D. Y. Kim, and T. W. Kang, "Ultrathin VS_2 nanodiscs for highly stable electro catalytic hydrogen evolution reaction," *International Journal of Energy Research*, vol. 44, no. 2, pp. 811–820, 2020.

[43] J. Ge, X. Ding, D. Jiang, L. Zhang, and P. Du, "Efficient improved charge separation of FeP decorated worm-like nanoporous $BiVO_4$ photoanodes for solar-driven water splitting," *Catalysis Letters*, vol. 151, no. 5, pp. 1231–1238, 2021.

[44] G. Mohan Kumar, H. D. Cho, P. Ilanchezhiyan et al., "3D flexible $W_xV_{1-x}Se_2$ nanoplates arrays on carbon cloth as an novel efficient hydrogen evolution electrocatalysts," *Applied Surface Science*, vol. 540, article 148297, 2021.

[45] D. J. Lee, G. Mohan Kumar, S. Sekar, H. C. Jeon, D. Y. Kim, and P. Ilanchezhiyan, "Ultrasonic processing of WO_3 nanosheets integrated Ti_3C_2 MXene 2D-2D based heterojunctions with synergistic effects for enhanced water splitting and environmental remediation," *Ultrasonics Sonochemistry*, vol. 101, p. 106681, 2023.

[46] H. D. Cho, P. Ilanchezhiyan, G. Mohan Kumar, and D. Y. Kim, "Highly carbonized tungsten trioxide thin films and their enhanced oxygen evolution related electrocatalytic functions," *Journal of Materials Research and Technology*, vol. 12, pp. 2216–2223, 2021.

[47] Y. Luo, G. Tan, G. Dong, H. Ren, and A. Xia, "A comprehensive investigation of tetragonal Gd-doped $BiVO_4$ with enhanced photocatalytic performance under sun-light," *Applied Surface Science*, vol. 364, pp. 156–165, 2016.

[48] T. Tokubuchi, R. I. Arbi, P. Zhenhua, K. Katayama, A. Turak, and W. Y. Sohn, "Enhanced photoelectrochemical water splitting efficiency of hematite (α-Fe_2O_3)-based photoelectrode by the introduction of maghemite (γ-Fe_2O_3) nanoparticles," *Journal of Photochemistry and Photobiology A: Chemistry*, vol. 410, article 113179, 2021.

[49] T. Soltani and B. K. Lee, "Ag-doped $BiVO_4/BiFeO_3$ photoanode for highly efficient and stable photocatalytic and photoelectrochemical water splitting," *Science of The Total Environment*, vol. 736, article 138640, 2020.

[50] U. Lamdab, K. Wetchakun, S. Phanichphant, W. Kangwansupamonkon, and N. Wetchakun, "$InVO_4$–$BiVO_4$ composite films with enhanced visible light performance for photodegradation of methylene blue," *Catalysis Today*, vol. 278, pp. 291–302, 2016.

[51] F. Guo, W. Shi, X. Lin, X. Yan, Y. Guo, and G. Che, "Novel $BiVO_4/InVO_4$ heterojunctions: facile synthesis and efficient visible-light photocatalytic performance for the degradation of rhodamine B," *Separation and Purification Technology*, vol. 141, pp. 246–255, 2015.

[52] Y. Zhou, L. Liu, T. Wu et al., "Flake-like $InVO_4$ modified TiO_2 nanofibers with longer carrier lifetimes for visible-light photocatalysts," *RSC Advances*, vol. 8, no. 48, pp. 27073–27079, 2018.